

LBLN FORGE Project 3-2535 Task 6 Milestone Report

Seismic Data Processing

Roland Gritto, EMR Solutions and Technology, Berkeley, CA

Steve Jarpe, Jarpe Data Solution Inc., Prescott Valley, AR

1. Introduction

In FORGE project 3-2535, EMR Solutions Technology (EMR) and Jarpe Data Solution (JDS) processed seismic data collected during the April 2024 stimulation by the Utah FORGE operator. Seismic P- and S-wave phase arrivals were determined using the software packages PhaseNet and GaMMA. The former was developed specifically for the processing of phase arrivals of seismic waves, while the latter is used for event association and preliminary event location. As part of the data processing, preliminary earthquake hypocenter solutions were determined. The phase data were then tomographically inverted to estimate the double difference hypocenter locations of micro-seismicity within the activated fracture reservoir and the 3D structure of the P- and S-wave ratio V_p/V_s . The goal was to assess the location and possibly the aggregate of the injectate in the basement rock. To support the tomographic results, double difference Wadati (DDW) analyses of the seismic data was conducted to estimate the V_p/V_s ratio in the stimulated fracture network.

2. Seismic Data Processing

In April 2024 the earthquakes induced by the stimulation of the basement rock were recorded by a suite of seismic and strain recorders. These included a three-component geophone string and a single three-component geophone of Geo Energy Swiss (GES) deployed in wells 78B and 56, respectively, and a three-component geophone string by Schlumberger (SLB) in well 58. Additionally, DAS strings were deployed and operated by Silixa in wells 16B and 78B. However, due to recording problems the SLB data were not made available.

Seismic data processing was conducted with software based on AI. The processing routines included PhaseNet (Zhu and Beroza, 2019), a deep-neural-network-based seismic arrival-time picking method and the Gaussian Mixture Model Association (GaMMA), an event association and preliminary location module. PhaseNet is based on deep-neural-network architecture and was trained with data consisting of thousands of analyst picks of California earthquake data. PhaseNet uses three-component seismic waveform data as input and generates probability distributions of P-wave and S-wave arrivals as output. The maxima in the probability distributions provide accurate arrival times for both P- and S-waves. It has been shown that PhaseNet is applicable to earthquakes in areas other than California (Zhu, 2022, personal comm.) The P- and S-wave phase arrivals are subsequently passed to GaMMA and analyzed for association with a seismic event and its preliminary location determined. GaMMA uses a grid search by which it progresses through grid points in the subsurface using FORGE basement rock velocities and computing time steps along waveforms to associate detections from PhaseNet as preliminary event detections. The

output of GaMMA includes preliminary event locations and P- and S-wave phase arrivals at those stations that recorded the event. All parameters are loaded into a database and input files are generated for tomographic imaging with the inversion code tomoFDD (Zhang and Thurber, 2006; Gritto et al., 2013). In addition to these input files, waveform cross correlations between events are computed for differential travel times and included in the inversion.

At the onset of seismic data processing, the FORGE team provided the seismic data recorded by the GES geophone string in well 78B and by the single GES geophone in well 56. However, the geometry of the seismic data sensors consisting of an eight-level geophone string and a single geophone was insufficient to yield reliable earthquake hypocenter locations. Therefore, we contacted Prof. Jonathan Ajo-Franklin of Rice University to inquire about the availability of the DAS data recorded in wells 16B and 78B. Professor Ajo-Franklin was gracious enough to provide the DAS data for seismic travel time analysis and subsequent tomographic imaging.

Because PhaseNet was developed for earthquakes, recorded by three-component seismic sensors, it is not optimized for DAS data, which comprises both P- and S-waves recorded by the same fiber strands in the direction of the cable. Therefore, we first tried the adapted code PhaseNet-DAS. PhaseNet-DAS was developed for DAS data but has not been trained on borehole data yet. Therefore, the code proved unsuccessful to analyze the DAS borehole data forcing us to return to the original PhaseNet package. Initial attempts to apply PhaseNet to the DAS data did not yield optimum results, therefore, we used the origin times from seismic catalog developed by the Univ. of Utah (Niemz et al., 2023) to compute narrow time windows in which we searched for P- and S-wave arrivals. Using this approach, we were able to obtain satisfactory P- and S-wave travel times from the geophone and DAS data. The data processing yielded 743 earthquakes with 12,576 P- and S-wave phase arrival times. These data and the preliminary event locations were subsequently used for 3D tomographic imaging.

3. 3D Tomographic Imaging

The phase data and preliminary earthquake locations were used in a joint inversion to derive earthquake hypocenter locations and 3D distributions of the P- and S-wave velocity ratio in the basement rock. The inversion code tomoFDD (Zhang and Thurber, 2006; Gritto et al., 2013) takes advantage of dynamic memory allocation, which enables allocation and deallocation of memory for any field or array as they are accessed during computation. The advantage is that larger data arrays can be assigned during the inversion, because most are not accessed simultaneously. Dynamic memory allocation and the use of the fast finite difference eikonal solver (Podvin and Lecomte, 1991) make tomoFDD well suited for the current project where the high number of DAS stations and a high number of inversion nodes pose demands on computer memory and CPU speed. The inversion with tomoFDD for the current project is based on a node spacing of 125 m, which provides sufficient resolution for reservoir-wide imaging and the goals of the current project.

The program tomoFDD uses damped least-squares to solve the inverse problem. One of the most important parameters to solve the system of equations is damping. The correct damping will generate the best compromise between reduced data variance and a smooth but geologically

reasonable model. The damping depends on the geometry of the system, such as the number and locations of seismic stations and the number and hypocenters of earthquakes. For each dataset the appropriate damping needs to be determined iteratively. In the current example, we ran multiple inversions with different damping parameters. For each damping parameter the variances of the data and the resulting slowness model are calculated and graphically displayed. The resulting curve is presented in Figure 1, which represents the results of 10 inversion runs. The graph shows the variance between the observed and calculated travel time as a function of slowness variance. Slowness variance is calculated from the differences between the starting and resulting slowness models. The ideal damping parameter is found by the point on the curve that offers the best compromise between small time and slowness variance. The best compromise is often associated with the point on the curve closest to the crossing of the two axes. In the current case, a damping parameter of 500 was chosen.

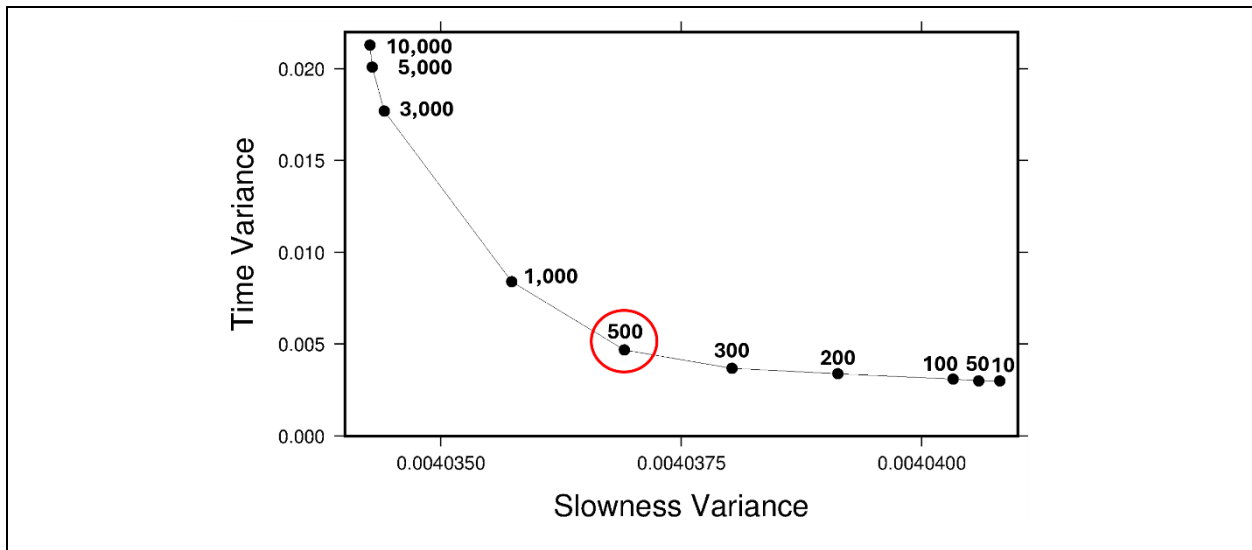
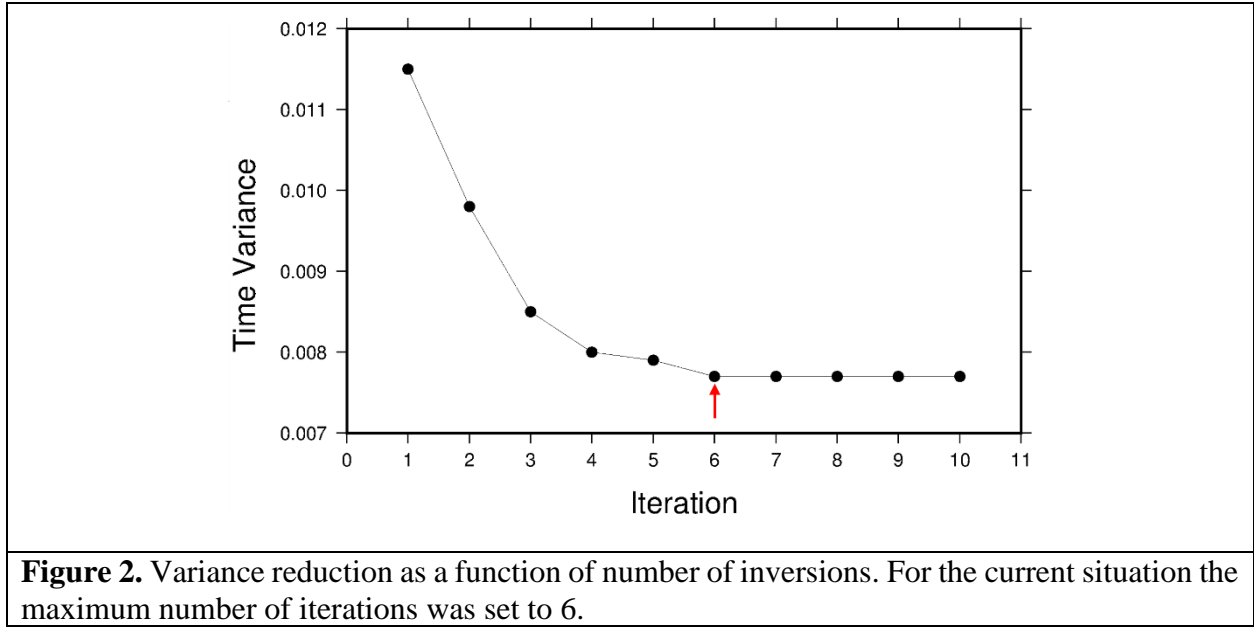


Figure 1. Trade-off curve for data and slowness variance to estimate the best damping parameter for the inverse problem. The red circle indicates the damping with best compromise between time and slowness variance.

Once the damping parameter is determined, the number of iterations the inversion is run to solve the system of equations is determined. The goal is to reduce the time variance between observed and numerically calculated travel time. Once the variance appears stable the inversion is stopped, because additional iterations would generate a velocity model that becomes too heterogenous and geologically unreasonable. In the current situation the maximum number of iterations was limited to six.



The 3D inversion of the seismic data was based on a node spacing of 125 m in horizontal and vertical direction and covered a depth range from 0 km - 8.0 km. The starting model was the 3D velocity model developed under the current project for the FORGE site (Gritto et al., 2023). It included a layered westward dipping sedimentary sequence, overlaying a basement with homogeneous velocity structure.

After inversion, the earthquake epicenter locations are presented in Figures 3 and 4. A cloud of earthquakes can be seen in Figure 3 cutting through the FORGE site and extending north and south of wells 16A and 16B. Figure 4 presents east-west and north-south cross sections through the FORGE site with the borehole trajectories and earthquake hypocenter locations. The hypocenter locations are well constrained in the vertical direction between depths of 2.0 km – 2.5 km.

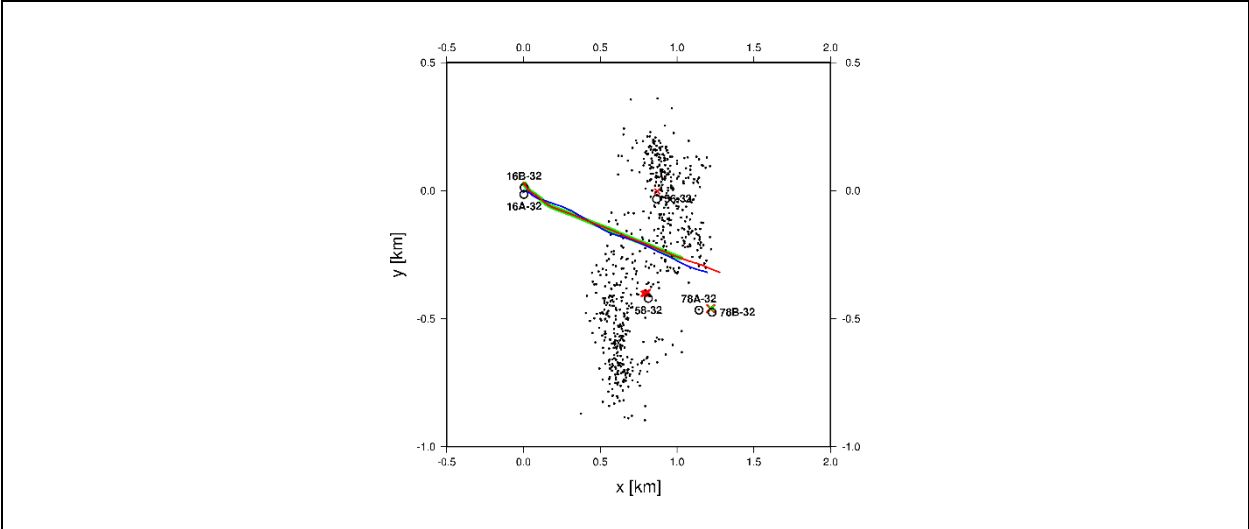


Figure 3. Map with the locations of boreholes at the FORGE site and earthquake epicenters (black dots) after inversion of the seismic data. The trajectories of boreholes 16A and 16B are given by the blue and red line, respectively. The location of the DAS cable in well 16B is indicated by the green line, while the borehole geophone locations and the DAS cable in well 78B are indicated by the red and green crosses, respectively.

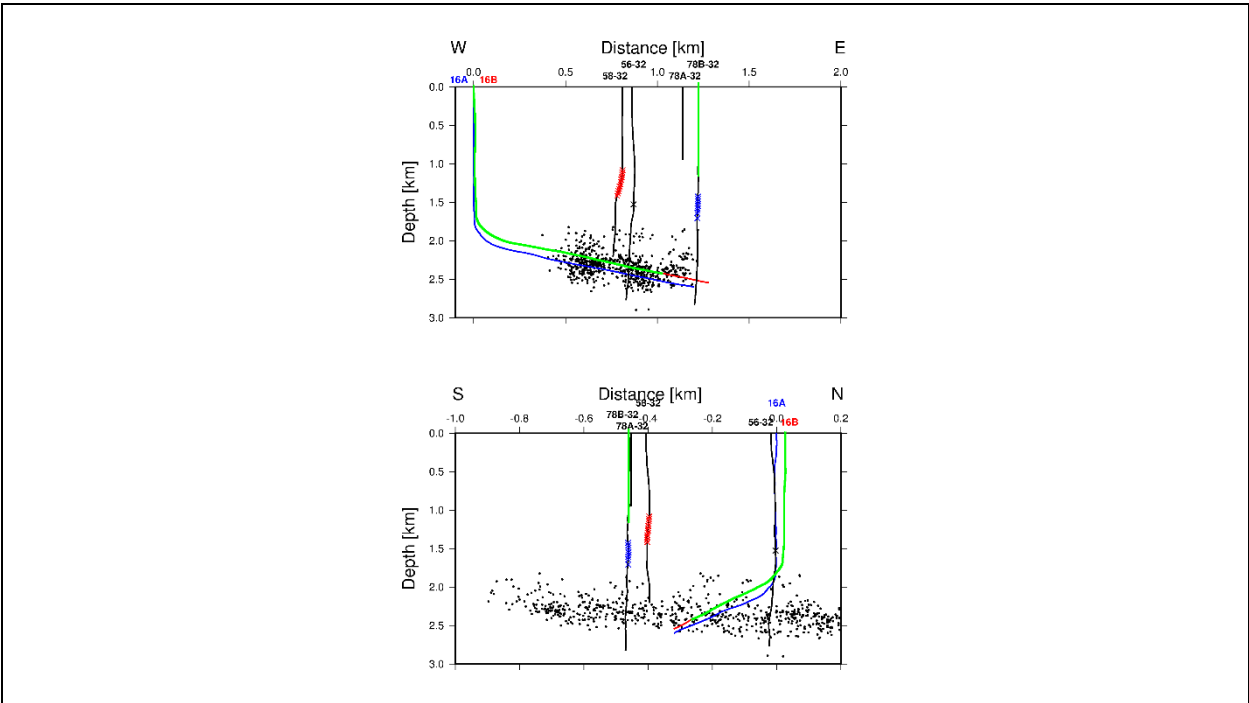


Figure 4. East-west (top) and north-south (bottom) cross sections with the locations of boreholes at the FORGE site and earthquake epicenters (black dots) after inversion of the seismic data. The trajectories of boreholes 16A and 16B are given by the blue and red line, respectively. The locations of the DAS cable in wells 16B and 78B are indicated by the green lines, while the locations of the GES and SLB borehole geophone locations are indicated by the blue and red crosses, respectively.

The inversion estimates for V_p/V_s are presented in Figures 5 and 6. The results in Figure 5 are presented for horizontal depth intervals from 2.0 – 2.65 km. Estimates are only plotted for nodes that have sufficient ray coverage as determined by the derivative weight sum (DWS). The V_p/V_s estimates in Figures 5 and 6 are presented on a scale from 1.4 to 2.0. For a perfectly elastic rock, without fractures, the V_p/V_s ratio is assumed to be 1.73. It is generally accepted that V_p/V_s ratios below 1.73 may indicate the presence of gaseous liquids in the formation, such as steam or gases in geothermal regions, while values above 1.73 may indicate the presence of fluid liquids such as for water-saturated rocks.

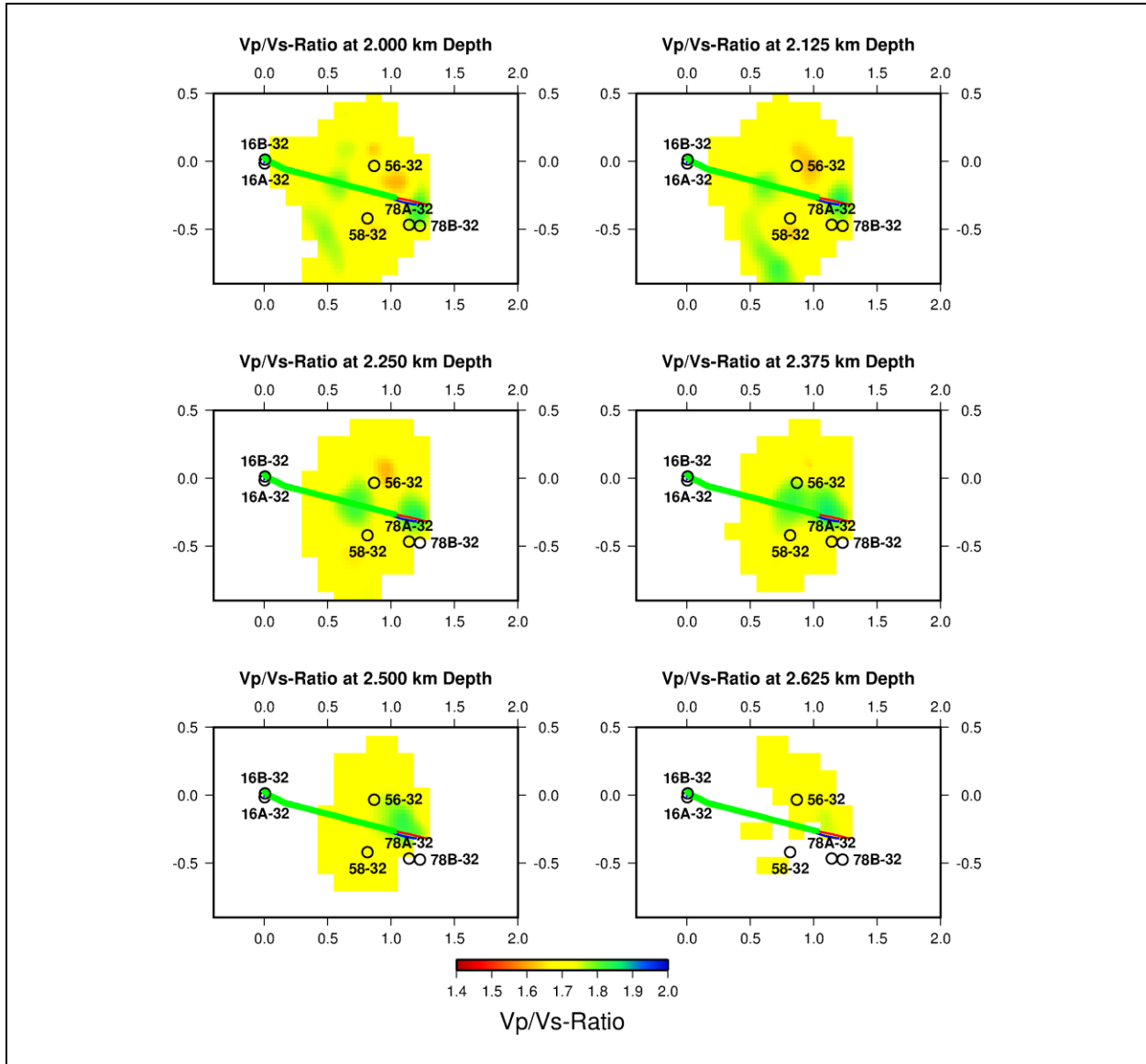


Figure 5. Horizontal slices of the V_p/V_s -ratio estimates from travel time inversion of the seismic data collected during the April 2024 stimulation. The estimates are only shown for regions that have sufficient ray coverage as determined by the derivative weight sum (DWS). Boreholes are shown for reference and the horizontal depths are indicated in the title of each panel.

At 2.0 km depth, the V_p/V_s ratio at the toe of well 16A suggest the presence of an anomaly above 1.8, which dominates the region surrounding the last 200 m of the borehole. At 2.25 km depth a second anomaly with values above 1.8 becomes visible below well 16A at $x \sim 0.7$ km. The two anomalies appear to merge at 2.375 km depth. These could be interpreted as two stages of the stimulation experiment, suggesting that the injectate is still fluid at the time of the induced seismicity. This is reasonable considering that the seismicity occurs concurrently with the injection of the fracturing fluid.

East-west cross sections with V_p/V_s estimates are presented in Figure 6. All cross sections are located south of the surface location of well 16A. The first two panels, located 0.166 km and 0.291 km south of the surface location of well 16A, reveal a V_p/V_s anomaly above 1.8 which appears to extend up along wells 16A and 16B towards the West and upwards above the toes of wells 16A and 16 B towards the East. If these anomalies are associated with liquid fluids, the injectate appears to have migrated upwards in the basement rock. An alternative interpretation could be the mixing of an upward migrating plume of injectate with liquid formation fluids naturally occurring in the basement rock at shallow depth. The two southernmost east-west cross sections do not indicate the presence of liquid fluid in the vicinity of wells 16A and 16B.

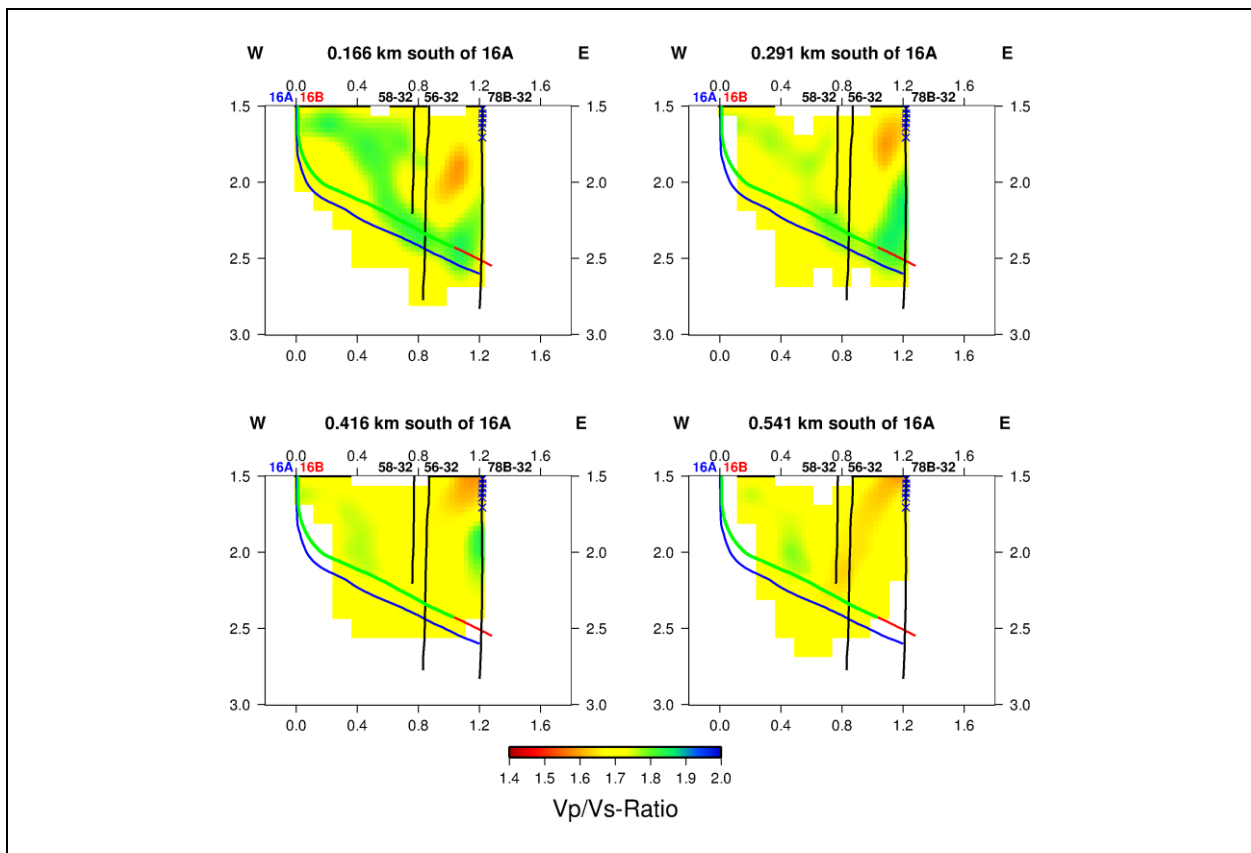
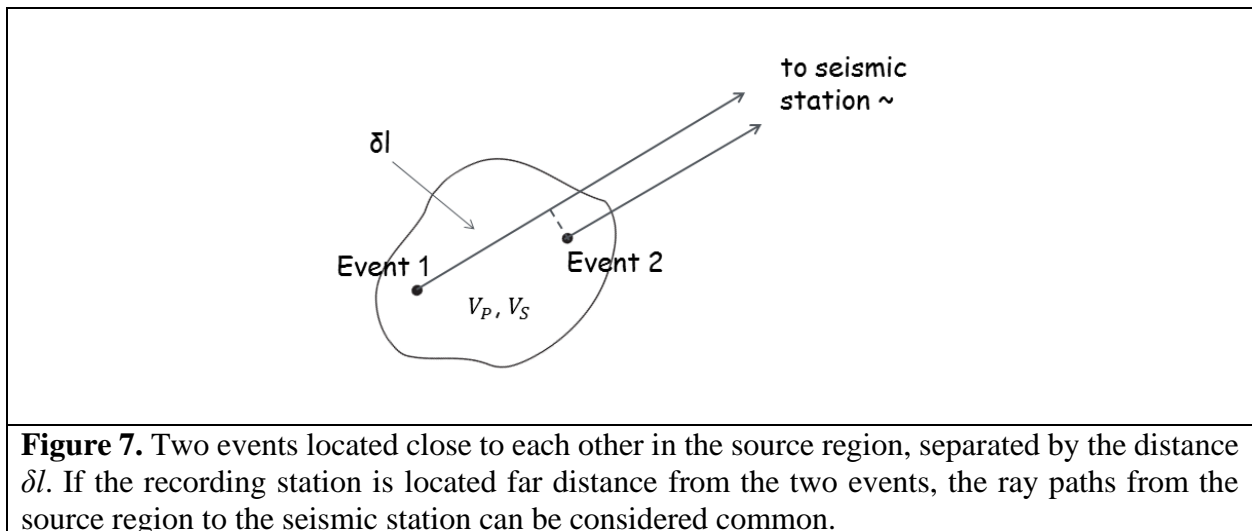


Figure 6. East-west cross sections of the V_p/V_s -ratio estimates from travel time inversion of the seismic data collected during the April 2024 stimulation. The estimates are only shown for regions that have sufficient ray coverage as determined by the derivative weight sum (DWS). The locations of the cross sections relative to the surface location of well 16A are indicated in the title of each panel.

4. Wadati Analysis

Wadati diagrams are useful to determine origin times of earthquakes and to estimate V_p/V_s ratios within earthquake clusters. The Wadati technique has been applied to estimate temporal changes of fluid distribution in fault zones (Lin and Shearer, 2007, 2009), in volcanic regions (Dahm and Fischer, 2013), and in geothermal reservoirs (Gritto et al., 2016). The advantage of using differences of P- and S-wave travel times between neighboring events is that medium effects along the common propagation paths from the events to a common seismic station are eliminated, which allows to estimate the V_p/V_s ratio in the near source region with higher accuracy than tomographic methods. In the present case, we applied the Wadati technique to P- and S-wave differential travel times to estimate fluid saturation in the fracture network based on V_p/V_s -ratio.

The concept of the Wadati method is illustrated in Figure 7, where two events are located close to each other in a source region at a far distance from the seismic recording stations. Due to the geometrical constraints the ray paths outside the source region to the recording station can be considered equal, while the separation distance between the events in the source region can be defined as δl . By differencing the P- and S-wave travel times of the seismic waves from the two events to the recording station, the effects of the medium along the propagation paths outside the source region are canceled. As a result, the slope of the differential travel times, plotted on a Wadati diagram, yields an estimate of the V_p/V_s ratio within the earthquake region.



The database of 743 earthquakes with 12,576 P- and S-wave phase arrival times was used to compute differential P- and S-wave travel times between neighboring events recorded by the same seismic station. The maximum separation distance between neighboring earthquake pairs was limited to 100 m. This yielded over 27,000 pairs of differential dt_p and dt_s travel times that were subsequently displayed on a Wadati diagram, the results of which are shown in Figure 8. The plot represents the differential travel times associated with the earthquake cluster that was induced during the April 2024 stimulation.

Estimating V_p/V_s ratio from Wadati diagrams requires accurate fitting techniques, since the differential travel times of the seismic waves propagating from neighboring events to a common recording station can be quite small. Therefore, we used the robust L1-L2 norm fitting technique to estimate the V_p/V_s ratio from differential travel times of earthquakes recorded during the April 2024 stimulation on a Wadati diagram. The L1-L2 technique allows the downweighting of outliers of travel time differentials that are always present in travel time data by using the L1 norm, and to fit more precise data points with the L2 norm. The best fit of the data cloud with the L1-L2 fitting technique yielded a slope of 1.86 ± 0.03 , which is indicated by the red line in Figure 8. If the assumption that the earthquakes are co-located within the stimulated fracture network is correct, the Wadati analysis suggest an average V_p/V_s ratio of 1.86 ± 0.03 in the fracture network, which matches the observed V_p/V_s estimates in the tomographic imaging results.

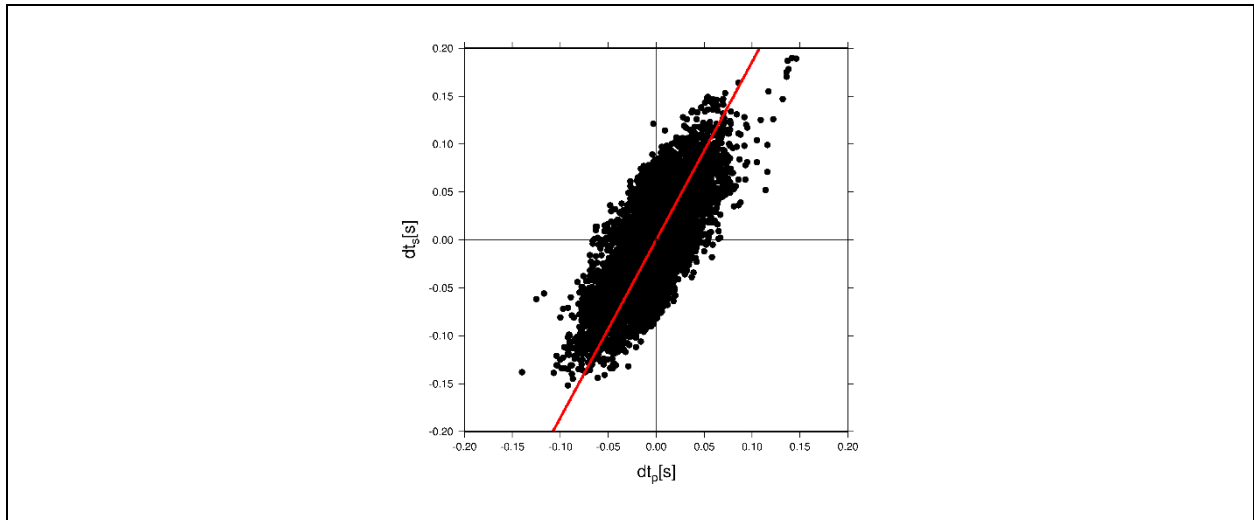


Figure 8. Wadati diagram with differential P- and S-wave travel times from neighboring events within the earthquake cluster induced during the April 2024 stimulation.

5. Conclusions

Initial processing of seismic data indicated that the GES sensors alone are insufficient to generate reliable earthquake hypocenter locations. This raised the need to supplement the seismic data recorded by the GES sensors by data recorded by the DAS cables in wells 16A and 78B. However, seismic DAS data require specific software for seismic phase identification, because P- and S-wave are recorded by the same fiber strands in the direction of the cable. The software package PhaseNet-DAS failed to pick phase data reliably as it has not been trained on borehole data yet.

Given the geometry at the FORGE site with earthquakes locating close to seismic sensors, travel time differences between P- and S-waves are small, which can lead to misidentification of the P- and S-wave phases. Additionally, overlap of event origin times and small hypocentral distances between events compound the problems of phase identification. However, these problems can

partly be sidestepped by using origin times of existing earthquake catalogs, such as the one published by the Univ. of Utah (Niemz et al., 2023), which was produced using an extensive network of surface and shallow borehole sensors.

In the current study, our earthquake hypocenter locations plot further west than the hypocenters in the Univ. of Utah catalog as presented in Figure 9 and 10. The mismatch might be caused by most phase picks being observed by the DAS string in well 16B, while the DAS string in well 78B did not contribute any phase picks to the dataset. The latter may be due to the extended distance of the 78B DAS string to the hypocenter locations and by being located in the higher attenuating sedimentary overburden. A disproportional distribution of seismic sensors located on one side of the earthquake clusters tends to skew the hypocenter locations towards those sensors.

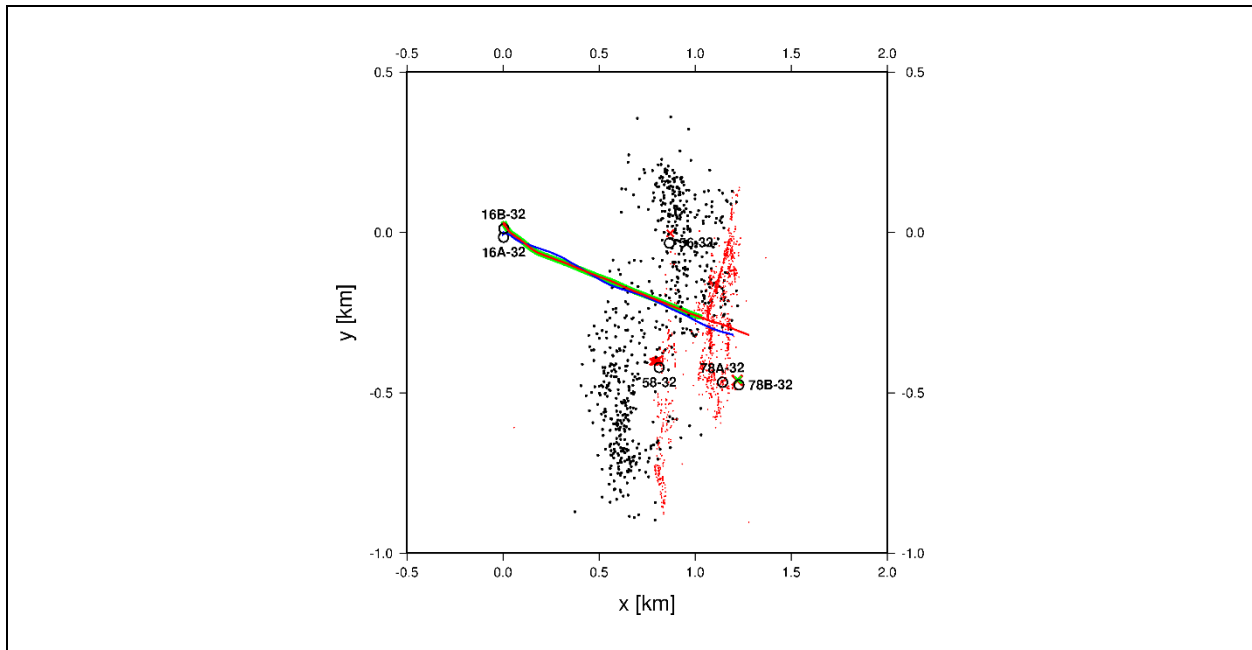


Figure 9. Map with the locations of boreholes at the FORGE site and earthquake epicenters of the current study (black dots) compared to the epicenter of the Univ. Utah catalog (red dots). The trajectories of boreholes 16A and 16B are given by the blue and red line, respectively. The location of the DAS cable in well 16B is indicated by the green line, while the borehole geophone locations and the DAS cable in well 78B are indicated by the red and green crosses, respectively.

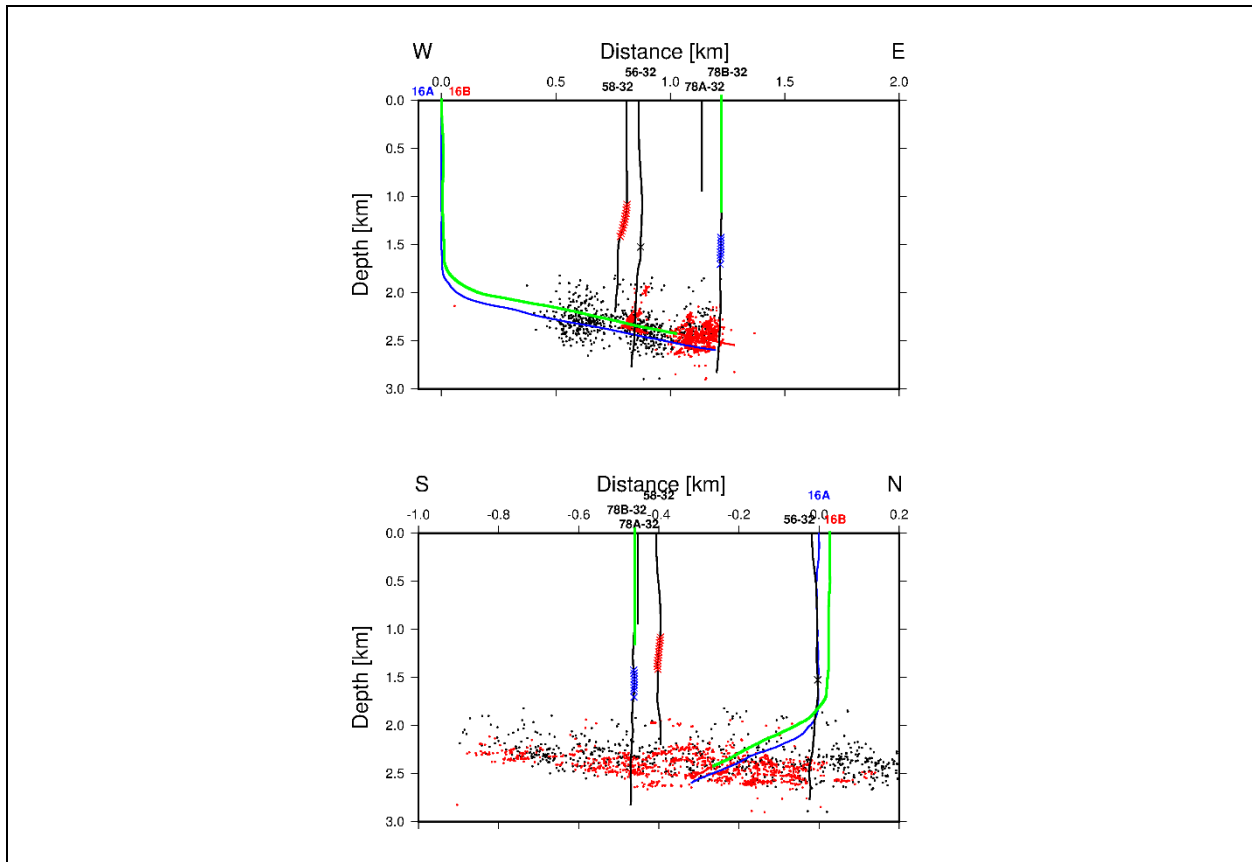


Figure 10. East-west (top) and north-south (bottom) cross sections with the locations of boreholes at the FORGE site and earthquake epicenters of the current study (black dots) compared to epicenters from the Univ. of Utah catalog (red dots). The trajectories of boreholes 16A and 16B are given by the blue and red line, respectively. The locations of the DAS cable in wells 16B and 78B are indicated by the green lines, while the locations of the GES and SLB borehole geophone locations are indicated by the blue and red crosses, respectively.

The 3D tomographic inversion of over 12,500 P- and 12,500 S-wave travel times yielded a distribution of V_p/V_s estimates that suggests the presence of two anomalies in the reservoir adjacent to wells 16A and 16B that may be linked to the presence of liquid fluid associated with the fracturing fluid injected during stimulation. This is a reasonable assumption, because the earthquakes occur concurrently with the injection of the stimulation fluid.

The Wadati analysis of over 27,000 pairs of differential P- and S-wave travel times supports this interpretation with a high V_p/V_s estimate of 1.86 ± 0.03 , averaged over the dimensions of the earthquake cluster.

6. References

- Dahm, T. and T. Fischer, 2013, Velocity ratio variations in the source region of earthquake swarms in NW Bohemia obtained from arrival time double-differences. *Geoph. J. Int.*, doi: 10.1093/gji/ggt410.
- Gritto, R., S.H. Yoo and S.P. Jarpe, 2013. Three-dimensional seismic tomography at The Geysers geothermal field, CA, USA, *Proceedings, 38th Workshop Geothermal Reservoir Engineering*, SGP-TR-198.
- Gritto, R., D.S. Dreger, O.S. Boyd, and T. Taira, 2016, Fluid Imaging, Moment Tensors and Finite Source Models During the EGS Demonstration Project at The Geysers, CA, *Proceedings, Stanford Geothermal Workshop*, 2016 Stanford University.
- Gritto, R. and D.W. Vasco, C. Chan, 2023. Development of a Reservoir Seismic Velocity Model, *Task 3 Milestone Report 3.1*, LBNL FORGE Project 3-2535, 1-15, <https://gdr.openei.org/submissions/1470>.
- Lin, G., and P.M. Shearer, 2007, Estimating local Vp/Vs ratios with similar earthquake 397 cluster, *Bull. Seism. Am.*, 97 (2), 379–388, 398, <http://dx.doi.org/10.1785/0120060115>.
- Lin, G., and P.M. Shearer, 2009, Evidence for water-filled cracks in earthquake source regions: *Geophys. Res. Lett.*, 36, L17315, doi:10.1029/2009GL039098.
- Niemz, P., Pankow, K., Isken, M. P., Whidden, K., McLennan, J., and Moore, J., 2025. Mapping fracture zones with nodal geophone patches: Insights from induced microseismicity during the 2024 stimulations at Utah, FORGE, *Seismological Research Letters*, 1-16, doi: 10.1785/0220240300.
- Podvin, P., and I. Lecomte, 1991. Finite difference computation of travel times in very contrasted velocity models: A massively parallel approach and its associated tools, *Geophys. J. Int.*, **105**, 271–284.
- Zhang, H. and C. H. Thurber, 2006. Development and Applications of Double-difference Seismic Tomography, *Pure Appl. Geophys.*, **163**, DOI 10.1007/s00024-005-0021-y, 373-403.
- Zhu W. and G. C. Beroza, 2019. PhaseNet: a deep-neural-network-based seismic arrival-time picking method, *Geophys. J. Int.*, **216**, 261–273, doi: 10.1093/gji/ggy423.